Journal of Materials Chemistry A

ROYAL SOCIETY OF CHEMISTRY

PAPER

View Article Online
View Journal | View Issue

Check for updates

Cite this: J. Mater. Chem. A, 2020, 8, 3333

A mechanistic study of mesoporous TiO_2 nanoparticle negative electrode materials with varying crystallinity for lithium ion batteries†

Changjian Deng,*[abc] Miu Lun Lau,[b] Chunrong Ma,[b] Paige Skinner,[b] Yuzi Liu,[d] Wenqian Xu,[e] Hua Zhou,[e] Xianghui Zhang,[f] Di Wu,[f] Yadong Yin,[g] Yang Ren,[e] Jorge Perez,[b] Diana Jaramillo,[b] Pete Barnes,[b] Dewen Hou,[b] Michael Dahl,[bg] Bethany Williford,[b] Chong Zheng[ac] and Hui (Claire) Xiong *[bh]

Nanoscale oxide-based negative electrodes are of great interest for lithium ion batteries due to their high energy density, power density and enhanced safety. In this work, we conducted a case study on mesoporous TiO_2 nanoparticle negative electrodes with uniform size and varying crystallinity in order to investigate the trend in the electrochemical properties of oxide-based nanoscale negative electrodes with varying crystallinity. Mesoporous solid spherical TiO_2 nanoparticles with a uniform particle size and varying crystallinity, *i.e.*, amorphous TiO_2 (A-TiO_2), partially crystalline TiO_2 (PC-TiO_2) and fully crystalline TiO_2 (FC-TiO_2) nanoparticles were studied. At low current rate (quasi steady-state), the specific capacity of the samples drops with the decrease of crystallinity. *Ex situ* synchrotron pair distribution function analysis reveals that the 1D zigzag Li ion diffusion pathway becomes expanded with the increase of crystallinity, which promotes ion mobility and charge storage. At high current rates (away from equilibrium states), however, the A-TiO_2 sample demonstrates slightly larger capacity than the FC-TiO_2 sample, both of which show larger capacities than that of the PC-TiO_2 sample. Both A-TiO_2 and FC-TiO_2 samples exhibit higher capacitive contribution to the charge storage and larger Li^+ diffusivity than those of the PC-TiO_2 sample, which explains their better rate capability. Moreover, the larger Li^+ diffusivity of the A-TiO_2 sample leads to the slightly larger specific capacity than the FC-TiO_2 sample at the highest current rate.

Received 13th November 2019
Accepted 19th January 2020

DOI: 10.1039/c9ta12499c

rsc.li/materials-a

Introduction

Lithium-ion battery (LIB) technology has dominated the markets for portable electronics and electric vehicles since it was first commercialized by Sony in 1991. Graphite is the state-of-the-art negative electrode material for LIBs due to its abundance, low production cost and reasonable theoretical capacity (372 mA h g^{-1}).[1,2] However, it suffers from significant structural collapse, exfoliation during cycling, lithium dendrite growth associated with its low operating voltage, and limitation for low-temperature applications.[1,3–8] The search for new negative electrode materials is pressing due to the fast development of LIB technology. Among various types of negative electrode materials, oxide-based intercalation-type negative electrodes are of great interest due to their high volumetric energy densities, enhanced safety and decent power densities.[2,9–14] Particularly, titanium-based oxide materials, *e.g.*, TiO_2, are attractive for lithium ion batteries because of their low cost, low toxicity, good theoretical capacity, safe operation potential (~1.7 V *vs.* Li/Li^+), low volume change during lithium insertion (<~4%), and high round trip efficiency.[2,12,15–18] The electrochemical properties of oxide electrode materials are largely influenced by the atomic arrangement. TiO_2 with various polymorphs have been investigated for LIBs, including anatase ($I4_1/amd$),[19–21] rutile ($P4_2/mnm$),[19,22,23] TiO_2-B ($C2/m$),[24,25] brookite ($Pbca$),[26] ramsdellite ($Pbmn$),[27] and hollandite ($I4/m$).[28] Among all of the polymorphs, anatase TiO_2 has been most extensively studied.[2,11,29] In addition

[a]Hoffmann Institute of Advanced Materials, Shenzhen Polytechnic, Shenzhen, 518055, China. E-mail: dcjduncan@hotmail.com

[b]Micron School of Materials Science and Engineering, Boise State University, Boise, ID 83725, USA. E-mail: clairexiong@boisestate.edu

[c]Department of Chemistry and Biochemistry, Northern Illinois University, Dekalb, IL, 60115, USA

[d]Center for Nanoscale Materials, Argonne National Laboratory, Lemont, IL, 60439, USA

[e]Advanced Photon Sources, Argonne National Laboratory, Lemont, IL, 60439, USA

[f]Voiland School of Chemical Engineering and Bioengineering, Washington State University, Pullman, WA 99164, USA

[g]Department of Chemistry, University of California – Riverside, Riverside, CA, 92521, USA

[h]Center for Advanced Energy Studies, 995 University Boulevard, Idaho Falls, ID, 83401, USA

† Electronic supplementary information (ESI) available. See DOI: 10.1039/c9ta12499c

to crystalline materials, nanostructured amorphous TiO_2 negative electrode materials show attractive electrochemical performance.[16] Xiong *et al.* investigated an amorphous TiO_2 nanotube (TiO_2NT) electrode and observed *in operando* an irreversible amorphous-to-crystalline phase transformation to a face-centered-cubic structure where Li and Ti are randomly distributed to share the same sublattice.[16] The newly-formed amorphous-to-cubic TiO_2NT showed high capacity, enhanced power, and long-term stability as compared to other TiO_2 polymorphs.[16] Several groups reported the electrochemical properties of both amorphous and crystalline TiO_2NT electrodes grown by electrochemical anodization and suggested that the amorphous TiO_2NT electrodes had better rate capability and cycle life than the crystalline ones.[30–32] However, limited work had been done in terms of systematic studies of the crystallinity effect in nanoscale TiO_2 electrodes with other morphologies.

In addition to Ti-based electrode materials, other oxide-based intercalation-type negative electrodes also exhibited the dependence of their electrochemical properties on the atomic arrangement, particularly on the intrinsic order and/or disorder characteristics. For example, orthorhombic molybdenum trioxide (α-MoO_3) delivered a reversible capacity of 450 mA h g^{-1} after 90 cycles.[33] On the other hand, amorphous MoO_3 shows a rapid decay in cycle-life performance ascribing to the massive volume change as well as repeated bond breaking and formation.[34] Moreover, molybdenum dioxide (MoO_2) with distorted rutile structure serves as a good host material for Li^+ intercalation with a theoretical capacity of 209 mA h g^{-1}.[35,36] Kim *et al.* modified the particle size of MoO_2 and obtained a reversible capacity of nearly 209 mA h g^{-1} after 100 cycles.[37] MoO_2 with even higher capacity (600 mA h g^{-1}) featured a disordered structure.[34] The extremely large capacity is related to the Li ion storage in the structural defects without severe volume change. Nevertheless, limited systematic work had been done to elucidate the effect of intrinsic order/disorder in oxide negative electrodes on their electrochemical properties.

Besides intrinsic atomic arrangement in oxide negative electrode materials, the order–disorder or disorder–order transitions could be initiated during the process of Li^+ intercalation, which also significantly influenced the corresponding electrochemical properties of oxide-based intercalation-type negative electrodes. It is well known that rutile TiO_2 undergoes order–disorder transitions upon deep discharge. Recently, Christensen *et al.* investigated the structural evolution of rutile TiO_2 nanoparticles using a combination of X-ray diffraction (XRD), X-ray scattering, TEM and pair distribution (PDF) analysis.[38] Their work elucidated the atomic-scale order–disorder transitions in rutile nanoparticles during cycling and revealed that rutile nanoparticles transformed into a composite of ~5 nm domains of layered Li_xTiO_2 with disordered grain boundaries upon Li intercaltion.[38] On the other hand, Xiong *et al.* had shown that Li^+ insertion into amorphous TiO_2 nanotubes triggered irreversible phase transition during the initial cycle from amorphous into a face-centered-cubic phase in the presence of a high concentration of Li ions (>75%).[16] In addition, the amorphous-to-cubic lithiated TiO_2 nanotube exhibited exceptional structural stability *via* a vacancy-filling mechanism under high pressure.[39] Furthermore, Yildirim *et al.* investigated the phase transition of 6 nm amorphous TiO_2 nanoparticles by molecular dynamics (MD) and suggested that Li diffusivity and segregation were enhanced with the increase of Li^+ concentration at the surface of the amorphous nanoparticle, leading to local atomic rearrangement and preferential crystallization.[40] However, such atomic rearrangement was not expected in anatase TiO_2 nanoparticles.[40] Nevertheless, to the best of our knowledge no experimental work has been reported regarding the crystallization in amorphous TiO_2 nanoparticles as observed in the TiO_2 nanotube system.[16] What is the reason behind that leads to the difference in the two nanoscale TiO_2 systems is not fully understood.

Although ordered and disordered oxide-based intercalation-type negative electrodes had been *independently* studied, the study of the trend of crystallinity in oxide electrodes on their electrochemical properties was limited. To this end, we conducted a systematic case study of mesoporous TiO_2 nanoparticle electrodes with uniform particle size and varying crystallinity trying to address the fundamental question regarding how crystallinity influences the electrochemical properties of oxide-based intercalation-type negative electrodes. We prepared amorphous TiO_2 (A-TiO_2), partially-crystalline TiO_2 (PC-TiO_2) and fully-crystalline TiO_2 (FC-TiO_2) nanoparticle samples through a water-assisted crystallization process[41] with uniform particle size and morphology and investigated the effect of crystallinity in TiO_2 nanoparticle negative electrode materials for LIBs. The crystallinity and morphology of the TiO_2 nanoparticles were characterized by XRD and transmission electron microscopy (TEM). The electrochemical properties of TiO_2 samples were evaluated as well. At low current rate, the specific capacity of the electrodes follows the trend that higher crystallinity leads to better capacity, which is possibly associated with more available storage sites in highly crystalline sample compared to the less-ordered samples. Moreover, it could be related to the lack of migration paths in disordered samples.[42] Interestingly, at high current rates, the electrodes show different trend with A-TiO_2 having a slightly larger capacity than FC-TiO_2, both of which show better capacities than that of the PC-TiO_2 sample. The electrochemical properties were investigated by cyclic voltammetry (CV) with varying scan rates, galvanostatic intermittent titration technique (GITT) along with thermogravimetric analysis/mass spectrometry (TGA-MS) and *ex situ* pair distribution function (PDF) characterization. It suggests that the low-rate (quasi steady-state) performance of mesoporous TiO_2 nanoparticle samples is related to the degree of crystallinity where higher crystallinity leads to higher capacity, which is associated with the reversible atomic rearrangements. On the other hand, at high current rates (away-from-equilibrium states) the charge storage and transport kinetics of mesoporous TiO_2 nanoparticle electrodes are related to pseudocapacitive processes and Li^+ diffusivity.

Experimental

Synthesis

The synthesis of uniform A-TiO_2 nanoparticles followed a sol–gel process reported previously.[41] PC-TiO_2 and FC-TiO_2 samples were prepared by subsequent water-assisted crystallization of A-TiO_2.[41] In brief, 0.85 mL of tetrabutyl orthotitanate (TBOT) was added to a mixture of 300 μL of sodium chloride (0.04 M), 0.15 g of hydroxypropyl cellulose (HPC), and 50 mL of 200-proof ethanol. The solution was stirred in air for 3 hours. The products were then centrifuged and washed with 200-proof ethanol and de-ionized (DI) water for several times. The sample was dispersed in the mixture of 19 mL of DI water and 1 mL of NaF solution (0.1 mg mL^{-1}), and then heated and stirred for 30 minutes at temperature of 50 °C, 75 °C and 100 °C for the A-TiO_2, PC-TiO_2 and FC-TiO_2 samples, respectively. The sample was finally washed with 200-proof ethanol, DI water, and then dried.

Characterization

XRD pattern were obtained by a Rigaku Miniflex 600 with Cu-Kα radiation ($\lambda = 1.5418$ Å) at a scan rate of 0.1°/s in the 2θ range of 20–80°. The morphology and microstructures were examined by TEM (FEI Titan 80-300 ST) at an accelerating voltage of 150 kV. TGA-MS measurements were carried out using a Netzsch STA 449 instrument (Netzsch, Selb, Germany). About 20 mg sample was pressed into a pellet and heated from 30 °C to 1000 °C (10 °C min^{-1}) under argon flow (40 mL min^{-1}). The surface area of TiO_2 materials was measured by nitrogen gas adsorption and desorption isotherms by a NOVA 3200e Quantachrome surface and pore size analyzer and calculated by the standard multi-point Brunauer–Emmett–Teller (BET) method. Synchrotron PDF experiments were performed at Beamline 17-BM at the Advanced Photon Source in Argonne National Laboratory. The X-ray wavelength was $\lambda = 0.24128$ Å. The samples used for PDF measurements were pristine or cycled laminated electrodes sealed in Kapton tape for immediate testing. A PerkinElmer a-Si area detector was used to collect 2D diffraction images in transmission mode. Image calibration and integration to 1D data of intensity *versus* 2θ was through program GSAS-II.[43] The 1D data in reciprocal space was subsequently converted to PDF profiles with program PDFgetX3.[44] XPS was conducted using an ESCALAB 250.

Electrochemical testing

The laminated electrodes were prepared by mixing a slurry of 80% of TiO_2 active materials, 10% of C65 carbon (Timcal America Inc.) and 10% of sodium carboxymethylcellulose (CMC, Dow Chemical Company). The slurry was cast on a copper current collector, vacuum baked at 100 °C overnight and punched into 1.5 cm dia. disc. The average mass loading of the electrode was ~0.8–1.0 mg cm^{-2}. The half-cell coin cells were assembled with TiO_2 electrode, Celgard 2325 separator, lithium (FMC) counter electrode in an electrolyte of 1.2 M lithium hexafluorophosphate ($LiPF_6$) in ethyl carbonate (EC) and ethylmethyl carbonate (EMC) (3 : 7 w/w) within an argon filled dry glove box (O_2 < 0.5 ppm). The coin cells were tested at various current rates with the potential window of 0.9 to 3 V on an Arbin battery tester. A three-electrode ECC-Ref (EL-CELL) cell was used to conduct CV at varying scan rates of 0.1–10 mV s^{-1}. It was also used for GITT. The electrode was discharged at a current rate of 10 mA g^{-1} for a 30 min pulse followed by a relaxation of 20 h to approach the steady state value. The process was repeated to the fully discharged state of 0.9 V. The electrochemical impedance spectroscopy (EIS) measurements were performed on an electrochemical workstation (Gamry Instruments, Reference 600).

Results and discussion

The samples with varying crystallinity were prepared by the water-assisted crystallization process reported previously.[41] The structure of the TiO_2 nanoparticles was investigated by XRD (Fig. 1). For A-TiO_2 sample, only broad bands were observed, indicating its amorphous feature. Both PC-TiO_2 and FC-TiO_2 samples can be indexed to anatase TiO_2 (JCPDS no. 21-1272). The peaks of PC-TiO_2 were significantly broader than those of FC-TiO_2, which suggests that PC-TiO_2 sample has lower crystallinity compared to FC-TiO_2. The (101) peak of the PC-TiO_2 sample was broad compared with that of the FC-TiO_2 sample, which is due to its smaller crystallite size (3.6 nm of PC-TiO_2 *vs.* 4.7 nm of FC-TiO_2) calculated by the Scherrer equation.[45] There was a slight rutile content in FC-TiO_2, which was indicated by the presence of rutile (110) peak at 30.6°. The weight percentage of the minor rutile phase was found to be 9% according to the analysis developed by Spurr *et al.*[46] Although there was minor rutile phase in the structure, its effect on the electrochemical properties of the FC-TiO_2 sample was not significant and its presence did not alter the crystallinity effect on TiO_2 nanoparticles, which is the main focus of this work.

The crystallographic and morphological properties of the samples were evaluated by TEM (Fig. 2). A-TiO_2 (Fig. 2a), PC-TiO_2 (Fig. 2b) and FC-TiO_2 (Fig. 2c) samples all maintained a mesoporous nanostructure with a uniform particle size of ~200 nm, consistent with our previous study.[41] Moreover, pore size analyzed by Barrett–Joyner–Halenda (BJH) model for A-TiO_2, PC-TiO_2 and FC-TiO_2 shows well-developed mesoporosity with very narrow pore size distributions (Fig. S1, ESI†). The

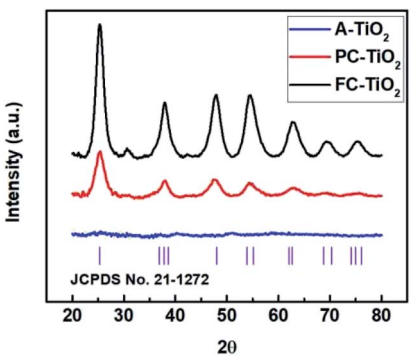

Fig. 1 X-ray diffraction patterns of TiO_2 nanoparticle samples.

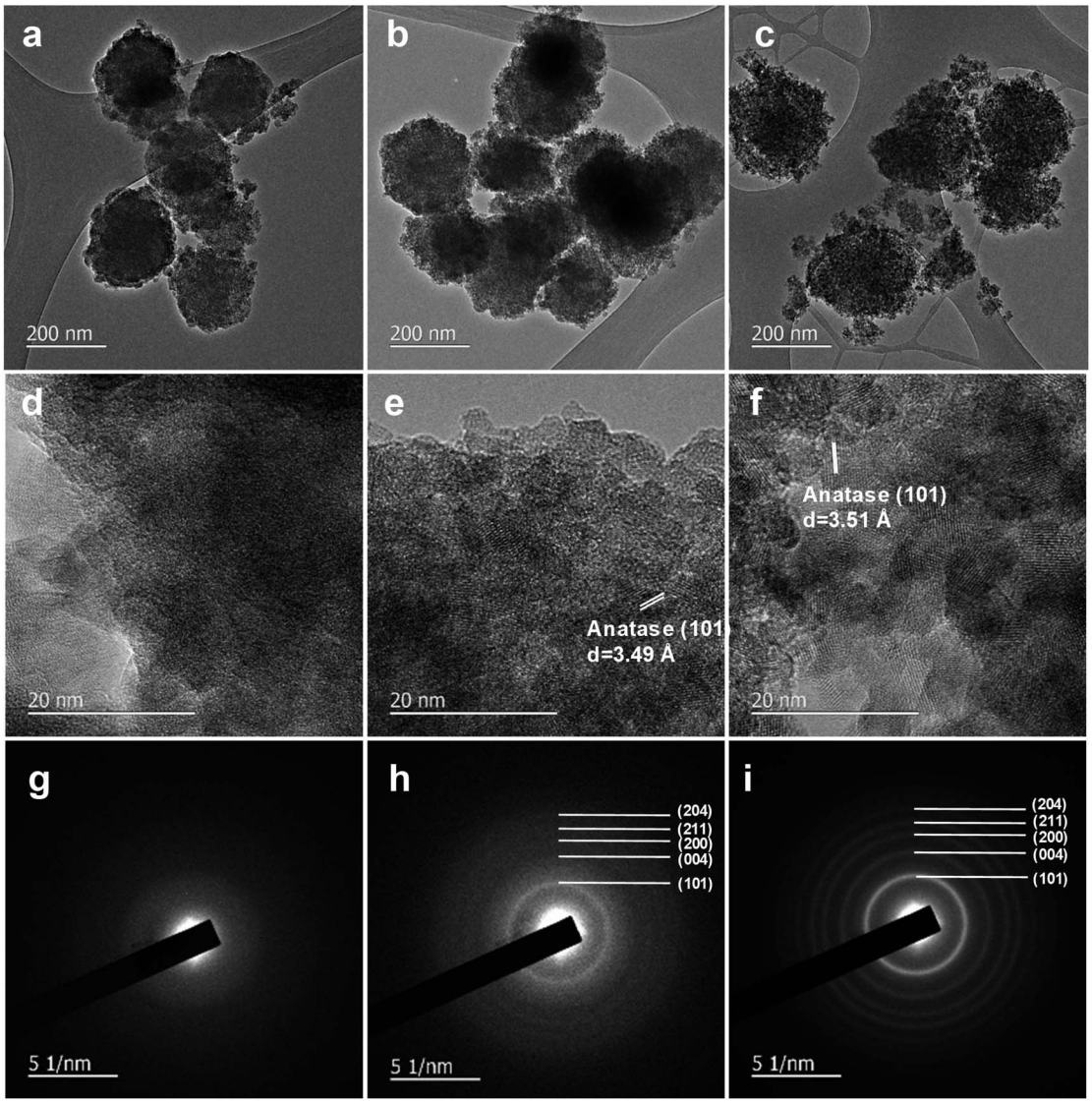

Fig. 2 TEM images of (a) A-TiO_2, (b) PC-TiO_2 and (c) FC-TiO_2. HRTEM images of (d) A-TiO_2, (e) PC-TiO_2 and (f) FC-TiO_2. And SAED patterns of (g) A-TiO_2, (h) PC-TiO_2 and (i) FC-TiO_2.

average pore size of A-TiO_2, PC-TiO_2 and FC-TiO_2 is 2.23, 3.26 and 5.03 nm, respectively. Both featureless high resolution TEM (HRTEM) image (Fig. 2d) and the characteristic diffuse ring in the selected area electron diffraction (SAED) pattern (Fig. 2g) suggest that there is no long-range order in the A-TiO_2 sample, which is consistent with the XRD result. The phase transformation to anatase phase in the PC-TiO_2 and FC-TiO_2 samples at elevated temperatures is attributed to the water-driven dissolution and re-precipitation/crystallization of TiO_6^{2-} octahedra.[40] For PC-TiO_2 sample, faint and broadened diffraction rings are present in the SAED pattern (Fig. 2h) where the corresponding planes are labelled. From the HRTEM image (Fig. 2e), it can be seen that PC-TiO_2 sample contains both amorphous and crystalline (anatase) domains. Both HRTEM and SAED results suggest that the PC-TiO_2 sample is partially crystalline. For FC-TiO_2 sample, the SAED pattern (Fig. 2i) exhibits well-defined diffraction rings of the anatase phase. HRTEM image (Fig. 2f) shows that the ~200 nm particle is composed of individual anatase grains (~5 nm) clustered together. Both HRTEM and SAED results suggest that FC-TiO_2 sample is crystalline. In addition, Raman spectroscopy (ESI, Fig. S2†) was conducted to evaluate the crystallinity of the three samples as it is sensitive to the crystallinity of materials. When the sample has local disorder or lattice imperfection Raman scattering weakens and the corresponding peaks broaden. FC-TiO_2 sample shows distinct signature peaks for anatase TiO_2 while A-TiO_2 exhibits no distinct peaks. For the PC-TiO_2 sample, most peaks disappear and the peak intensity of the $E_{g(1)}$ peak (148 cm^{-1}) dramatically decreases, suggesting the decrease of crystallinity. Results from XRD, TEM and Raman are consistent and indicate the crystallinity follow the trend: FC-TiO_2 > PC-TiO_2 > A-TiO_2.

Previous work[47] had shown that water could play a significant role in the charge storage kinetics of transition metal oxide

electrodes. Since our samples were prepared *via* a water-assisted crystallization process, it would be helpful to understand the role of water in each sample on their electrochemical properties. We conducted TGA-MS characterization to investigate the water content of the TiO_2 nanoparticle samples (Fig. 3). MS signal was observed for $m/z = 18$, corresponding to H_2O molecules. The desorption of H_2O species can be divided into two main regions: physically-adsorbed H_2O (loosely bound water) released at about ~120 °C and chemically-adsorbed H_2O (crystallographic water or strongly bound hydrates) released at ~300 °C.[48] Peaks in the DTG curves indicate temperatures where maximum rate of weight loss occurred. There are two peaks at ~120 °C and ~300 °C present for all three samples (Fig. 3a), corresponding to the physically-adsorbed and chemically-adsorbed H_2O release, respectively, consistent with the simultaneous MS peaks (Fig. 3b). The physically-adsorbed water content of A-TiO_2, PC-TiO_2 and FC-TiO_2 is 13.9%, 11.3% and 7.2%, respectively, and chemically-adsorbed water content is 10.0%, 8.0% and 6.6%, respectively. Both water content measurements follow the trend that the decrease of crystallinity leads to the increase of water content, which is consistent with the recent study that water adsorption on amorphous TiO_2 was energetically preferred over a crystalline TiO_2 surface.[49]

Fig. 4 shows the 1st cycle voltage profiles of TiO_2 samples at a low current rate of 20 mA g^{-1}. The discharge capacities of A-TiO_2, PC-TiO_2 and FC-TiO_2 are 360 mA h g^{-1}, 366 mA h g^{-1} and 305 mA h g^{-1}, with a corresponding coulombic efficiency of 45%, 49% and 64%, respectively. Wu *et al.* investigated the insertion of Li ions into the hydrogen titanate and TiO_2 structure and found that the large 1st cycle irreversible capacity was related to the side reaction between Li ions and adsorbed water due to the nanoscale TiO_2 samples.[50] For our samples, the 1st cycle coulombic efficiency of A-TiO_2 and PC-TiO_2 are much smaller than that of FC-TiO_2 sample, which can be attributed to the larger physically-adsorbed water (free water) content compared to the FC-TiO_2 sample (Fig. 3). Moreover, it is widely accepted that the 1st cycle coulombic efficiency is closely related to the surface area of nanomaterials, where high surface area leads to significant side reactions with the electrolyte and the formation of solid electrolyte interface (SEI) layer.[51,52] The BET surface area of A-TiO_2, PC-TiO_2 and FC-TiO_2 is 385, 366 and 251 m^2 g^{-1}, respectively, which helps to explain an improved coulombic efficiency with the increase of crystallinity. The correlation of the surface area and crystallization process has been well understood from our previous work.[41] The surface area of TiO_2 nanoparticle drops very quickly for the sample treated at 100 °C when the phase transformation starts much earlier, while it maintains a high value for the sample treated at 50 °C when the sample remains amorphous throughout the treatment period.[41] Based on the trend discovered in previous study[41] regarding surface area *versus* treatment time at the duration (30 min) used to heat-treat our samples, the surface area was very similar for A-TiO_2 and PC-TiO_2 sample. In addition, we had reported the characteristic "hump" at ~1.1 V *vs.* Li/Li^+ in the voltage profile of amorphous TiO_2 nanotube electrode during the first discharge indicative of an irreversible phase transition of amorphous TiO_2 to a cubic phase.[16] However, this "hump" feature was not observed in our A-TiO_2 sample, suggesting the absence of the phase transition. It is possibly

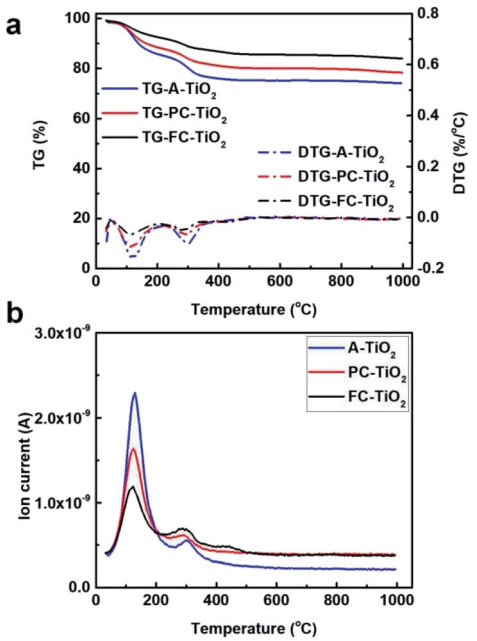

Fig. 3 (a) TG and DTG profiles and (b) MS profiles of TiO_2 samples.

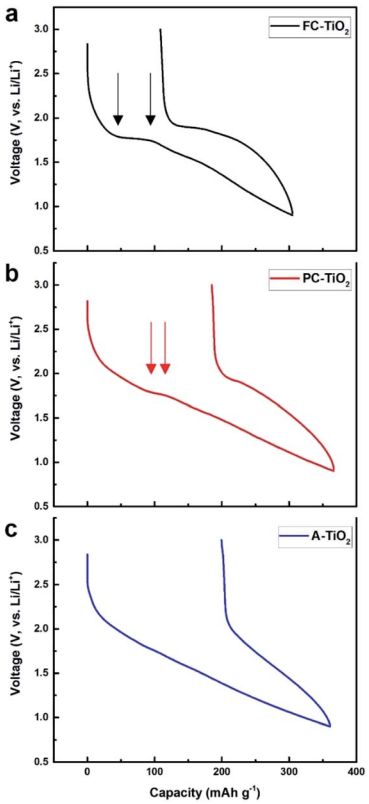

Fig. 4 1st cycle voltage profiles of (a) FC-TiO_2, (b) PC-TiO_2 and (c) A-TiO_2. The arrows highlight the length of the plateau in the discharge curve at 1.77 V.

because that: (1) the adsorbed water hindered the phase transition; (2) the particle size was too large to accumulate high enough concentration of Li ions (>75%) to initiate the phase transition; and (3) the formation of a thin SEI layer may hinder the crystallization. Indeed, a separate study is currently underway in our labs considering (a) the degree of hydration on the performance of TiO_2 polymorphs (FC, PC and A) using integrated thermodynamic (calorimetric), structural and performance investigations, (b) the particle size, and (c) the potential window and cycling rate. The work will be reported in subsequent publications.

There is a pronounced plateau at ~1.77 V and a subtle plateau at 1.57 V in the discharge curve of FC-TiO_2 sample, suggesting the phase transition from anatase to lithiated orthorhombic phase[53] and from lithiated orthorhombic phase to a Li-rich tetragonal phase,[54] respectively. The voltage plateau at 1.77 V is slightly higher than the typical observed value at ~1.7 V, possibly due to the defects within the crystalline structure.[17,55] The sloping curve can be attributed to single solid solution behavior. There is a markedly shorter plateau at 1.77 V in the discharge curve of PC-TiO_2 sample than that of FC-TiO_2 sample, suggesting less crystallinity in PC-TiO_2 compared to FC-TiO_2 with more defect sites. As for A-TiO_2, there is no apparent plateau, indicating the solid solution Li diffusion without phase transition.

The cycling stability of TiO_2 samples at a low current rate of 20 mA g^{-1} is shown in Fig. 5a. After 12 cycles the coulombic efficiency of FC-TiO_2 sample exceeded 99% while it took 17 and 25 cycles for PC-TiO_2 and A-TiO_2 sample to reach to the same level. After 100 cycles, the FC-TiO_2 delivered a reversible capacity of 168 mA h g^{-1}, which is larger than those of the PC-TiO_2 (125 mA h g^{-1}) and A-TiO_2 (111 mA h g^{-1}) sample. The reversible capacity of FC-TiO_2 sample is also comparable to the reported results.[56,57] The structural stability of cycled samples was examined by TEM (Fig. S3, ESI†). The cycled samples exhibited similar particle size and morphology (Fig. S3a–c†) as compared to pristine samples (Fig. 2a–c), maintaining structural integrity after extended cycles. From the HRTEM and SAED results (Fig. S3d–i†), the crystallinity of the cycled samples did not vary significantly upon cycling and still followed the trend as observed in the pristine samples (Fig. 2).

The rate capability of TiO_2 samples is shown in Fig. 5b. The capacity moderately drops with the increase of current rates and reversibly ramps back, suggesting the good capacity retention. All TiO_2 samples exhibit great rate capability under different current rates varying from 0.02 A g^{-1} to 2 A g^{-1}. Among all three samples, A-TiO_2 shows the best rate capability (Fig. 5c). It is worth noting that at the low current rate (0.02 A g^{-1}), the capacity of FC-TiO_2 is 17 mA h g^{-1} greater than that of A-TiO_2. The gap gradually decreases with the increase of current rate, which is 11 mA h g^{-1} at 0.1 A g^{-1} and 3 mA h g^{-1} at 0.5 A g^{-1}. When the rate is at 2 A g^{-1}, the A-TiO_2 (76 mA h g^{-1}) has slightly larger capacity than the FC-TiO_2 (71 mA h g^{-1}), both of which are much larger than that of PC-TiO_2 (61 mA h g^{-1}). At the low current rate of 0.02 A g^{-1}, the specific capacity decreases with the decrease of crystallinity, possibly because of more available active sites with the increase of crystallinity[58] under quasi steady-state and lack of migration paths in amorphous

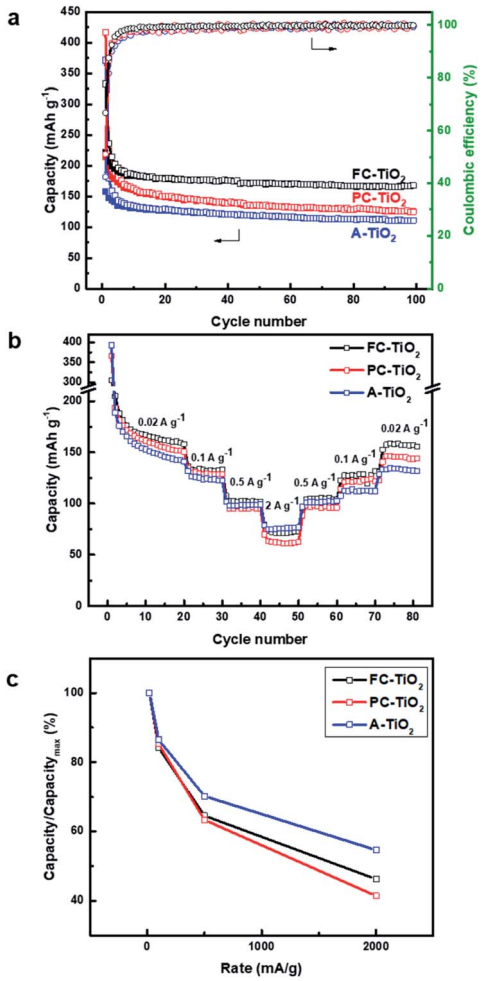

Fig. 5 Electrochemical performance of the electrodes: (a) cycle life (shown in discharge capacity), (b) rate capability; and (c) capacity *vs.* current rate of TiO_2 samples.

materials[42] might have led to reduced charge transport. However, this cannot be applied to explain the case of high current rate (2 A g^{-1}) (off-equilibrium state) where A-TiO_2 has larger capacity than FC-TiO_2, and PC-TiO_2 sample has the lowest capacity.

In order to understand the charge storage kinetics related to the rate capability observed in TiO_2 nanoparticle electrodes with different crystallinity, we conducted CV with varying scan rates (Fig. 6). Fig. 6a shows the CV curves of TiO_2 samples at a scan rate of 0.1 mV s^{-1}. The A-TiO_2 sample did not exhibit any apparent redox peaks, suggesting there was no phase transition during cycling. PC-TiO_2 sample had a pair of broad reduction and oxidation peak at 1.76 V and 2.04 V, respectively, attributable to the phase transition between anatase and the lithiated orthorhombic phase.[54] Moreover, the FC-TiO_2 sample showed a pair of distinct reduction and oxidation peak at 1.76 V and 1.98 V, suggesting the pronounced two-phase region.[17] The peak-to-peak separation of PC-TiO_2 sample (0.28 V) is slightly larger than that of FC-TiO_2 sample (0.22 V), indicating better kinetics in FC-TiO_2 electrode compared to PC-TiO_2 sample, consistent with the rate capability study.

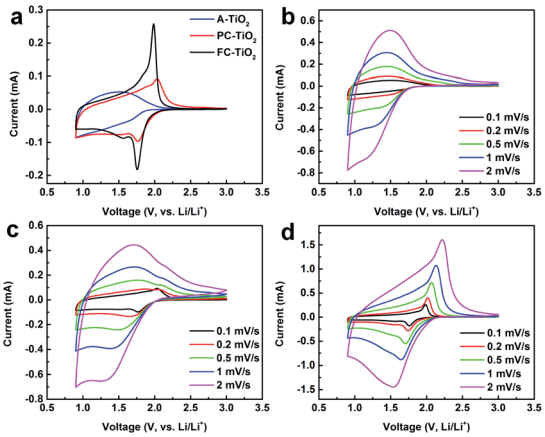

Fig. 6 (a) CV curves of TiO_2 samples at the scan rate of 0.1 mV s^{-1} with the voltage window of 0.9–3.0 V. The CV curves of (b) A-TiO_2, (c) PC-TiO_2 and (d) FC-TiO_2 at various scan rates.

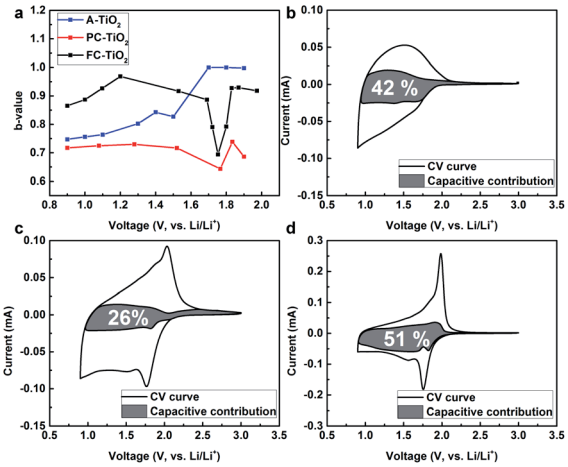

Fig. 7 (a) The *b*-value of TiO_2 samples. And the voltammetric response for (b) A-TiO_2, (c) PC-TiO_2 and (d) FC-TiO_2 at a scan rate of 0.1 mV s^{-1}. Shaded area: capacitive contribution.

The charge storage of nanoscale TiO_2 materials is related not only to diffusion-controlled intercalation, but also to surface capacitive processes associated with their high surface area and surface redox reactions.[59] The intercalation process is related to the solid-state diffusion of Li^+ in host materials, which can be sluggish because of low Li^+ diffusivity in solid. The surface capacitive process is mainly related to pseudo-capacitance and double layer effect, both of which contribute to the high-power performance due to the extremely rapid surface processes.[14,59] The effect of intercalation and capacitive processes can be quantitatively analyzed by interpreting CV data at various scan rates according to the power law relationship:[60]

$$i = av^b \quad (1)$$

where i is the measured current, v as the scan rate, a and b as adjustable parameters. There are two well-defined b values, where $b = 0.5$ and $b = 1$ indicate diffusion-limited intercalation process and surface capacitive process, respectively. The CV curves with various scan rates of A-TiO_2, PC-TiO_2 and FC-TiO_2 samples are shown in Fig. 6b, c and d, respectively. The plots of b value *vs.* voltage of TiO_2 samples during discharging (Li^+ insertion) at the scan rate of 0.1 mV s^{-1} are shown in Fig. 7a. The b values of PC-TiO_2 sample remain the lowest (~0.7) during the whole reduction process, suggesting the fraction of capacitive contribution in PC-TiO_2 is lower than that in A-TiO_2 and FC-TiO_2 samples, which leads to its low rate capability. There is a significant drop of b value when discharged from 1.83 V to 1.75 V for both PC-TiO_2 and FC-TiO_2 samples, which indicates the process is diffusion-controlled and can be attributed to the phase transition from anatase to the lithiated orthorhombic phase.[54] Below 1.75 V, the b-value significantly increases as the phase transition is completed, consistent with previous study.[59] At high voltages (>1.6 V), the b value of A-TiO_2 is close to 1, suggesting the dominant capacitive process, which is larger than that of FC-TiO_2. However, at low voltages (<1.6 V), the b value of A-TiO_2 (0.75–0.85) is smaller than that of FC-TiO_2 (0.85–1), which suggests more surface capacitive effect in FC-TiO_2 when more Li^+ ions are inserted in the solid-solution region.

In order to quantitatively determine the contribution of the diffusion-limited intercalation process and pseudocapacitive process during both reduction and oxidation process, we plotted the capacitive contribution (shaded area) in Fig. 7b, c and d for A-TiO_2, PC-TiO_2 and FC-TiO_2 according to the equation:[61,62]

$$i(V) = k_1 v + k_2 v^{1/2} \quad (2)$$

where the term $k_1 v$ and $k_2 v^{1/2}$ represent the contributions from surface capacitive and diffusion-controlled intercalation respectively. It was found that the capacitive contribution of PC-TiO_2 (26%) was significantly smaller than that of A-TiO_2 (42%) and FC-TiO_2 (51%), which is consistent with the b-value analysis and corroborated well with the rate capability study. The lower contribution of capacitive processes in PC-TiO_2 might relate to the accessible sites for Li^+ adsorption. PC-TiO_2 has mixed amorphous and crystalline domains, which may make some areas not accessible[17] even though its surface area is comparable to A-TiO_2.

In addition to the capacitive contribution to reaction kinetics, the rate capability is also dependent on diffusion-controlled intercalation process. Therefore, we evaluated the Li ion diffusion coefficient by galvanostatic intermittent titration technique (GITT) (Fig. 8a, details can be found in ESI†). The plot of the Li diffusivity as a function of voltage is shown in Fig. 8b. For the FC-TiO_2 sample, the diffusion coefficient significantly decreases when discharged from 1.91 V to 1.81 V, which is associated with the increased Li-ion diffusion barriers due to the reduction of Ti^{4+} causing the shortening of O–O pairs where Li^+ ions migrate.[63] From 1.81 V to 1.76 V, the diffusion coefficient increases due to the completion of phase transition from anatase to the lithiated orthorhombic phase.[54] Below 1.76 V, the diffusion coefficient decreases when discharged from 1.71 V to 1.62 V due to the solid solution lithiation within orthorhombic phase. Furthermore, it slightly increases when discharged from 1.62 V to 1.25 V due to the phase transition

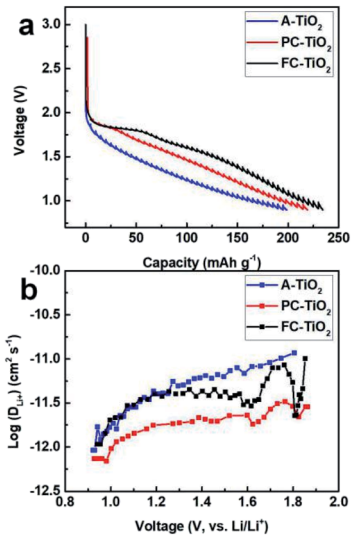

Fig. 8 (a) GITT profile and (b) diffusivity *vs.* state of charge of TiO_2 samples.

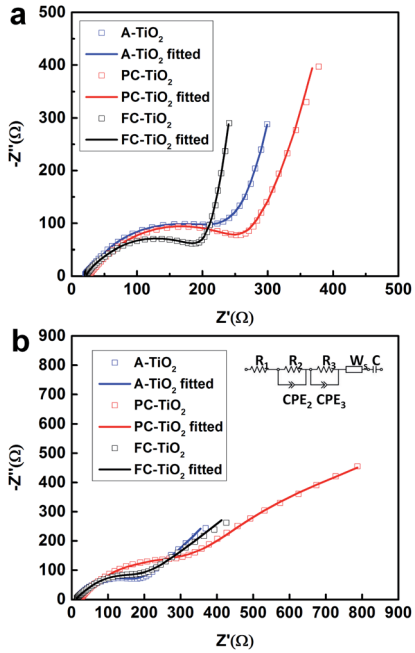

Fig. 9 EIS of (a) pristine and (b) 10th cycled TiO_2 samples. Inset: the equivalent circuit model.

from the orthorhombic phase to Li-rich tetragonal phase.[54] Finally, the diffusivity gradually decreases during the subsequent discharging process, as a result from the limited active sites when Li ions were continuously inserted into the TiO_2 host. The diffusion coefficient of PC-TiO_2 sample exhibits similar behavior with FC-TiO_2 sample, but the change is not as significant due to the partially-crystalline feature. As for A-TiO_2 sample, the diffusion coefficient gradually decreases within the whole voltage window due to the decrease in active sites as Li ions continue to occupy vacant sites in the host. It is worth noting that the diffusion coefficient of PC-TiO_2 sample is the lowest within the whole voltage window, indicating the slow intercalation process through multiple domains (amorphous/anatase) resulting in a reduced ion mobility.[17] The diffusion coefficient of FC-TiO_2 sample is smaller than that of A-TiO_2 sample when voltage is larger than 1.25 V, which might relate to the sluggish phase transition and subsequent diffusion in solid solution. When the voltages are smaller than 1.25 V, the FC-TiO_2 and A-TiO_2 samples have similar Li^+ diffusivity.

Electrochemical impedance spectroscopy (EIS) was conducted to investigate the kinetic properties of the electrodes. The Nyquist plots of pristine and 10th cycled TiO_2 samples are shown in Fig. 9a and b, respectively. These plots all exhibit convoluted semicircles followed by a straight line of Warburg-type region from high to low frequencies. The equivalent circuit model[64] used for fitting is shown in the inset in Fig. 9b. In this model, R_1 represents the bulk resistance of the cell. R_2 and CPE2 represent the resistance and constant phase element of the surface process at the electrodes. R_3 and CPE3 belong to the charge transfer process at the electrodes. W_s and C refer to the Warburg impedance and intercalation capacitance, respectively. From the results, R_2 of the pristine PC-TiO_2 sample (70 Ω) was larger than that of the pristine A-TiO_2 (58 Ω) and FC-TiO_2 sample (28 Ω). After cycling, R_2 of PC-TiO_2 sample (267 Ω) increased, while R_2 of cycled A-TiO_2 (37 Ω) and FC-TiO_2 sample (18 Ω) decreased. In addition, cycled PC-TiO_2 sample showed larger R_3 (175 Ω) than those from the cycled A-TiO_2 (95 Ω) and FC-TiO_2 sample (116 Ω). These results suggest that A-TiO_2 and FC-TiO_2 samples have facile surface processes and enhanced charge transfer kinetics compared to the PC-TiO_2 sample, which is consistent with their rate performance.

Considering the CV, GITT and EIS results, we were able to understand the rate performance of TiO_2 nanoparticle samples with varying crystallinity. At high current rate (2 A g^{-1}), the Li intercalation process is off-equilibrium and is rather limited by charge transfer and transport kinetics where greater capacitive contribution to the charge storage and faster Li^+ diffusion lead to higher specific capacity. PC-TiO_2 sample has the least capacitive contribution and smallest Li^+ diffusion coefficient, possibly because that mixed amorphous and crystalline domains presented more barriers for Li^+ transport and storage. Therefore, it exhibits the lowest specific capacity at high current rate. In contrast, A-TiO_2 sample with the largest Li^+ diffusivity and fairly high capacitive contribution delivers the highest capacity at high rate. On the other hand, FC-TiO_2 sample has the largest capacitive contribution but a smaller Li^+ diffusivity compared to A-TiO_2 sample. Therefore, FC-TiO_2 sample demonstrates a slightly lower capacity than A-TiO_2 sample at high current rate, suggesting diffusion-limited intercalation became significant for high-rate performance.

In addition to the electrochemical analysis, *ex situ* pair distribution function analysis (PDF) was conducted to investigate the structural evolution of TiO_2 samples. XRD characterization has been successfully used to analyze a variety of crystalline materials. However, materials with nanoscale crystallites or disordered structure usually exhibit diffuse Bragg-like peaks, which are neither as sharp nor as many as

those observed in the XRD patterns of regular bulk crystalline materials.[65] As a result, it is challenging to obtain structural information from highly disordered or nanoscale materials using standard XRD. This limitation of traditional XRD can be tackled by PDF.[65] The PDF patterns of as-prepared TiO_2 powder samples are shown in Fig. 10a. All samples showed well-defined structural features at small real-space distances. The features completely vanished at approximately 8 Å, 35 Å and 48 Å for A-TiO_2, PC-TiO_2 and FC-TiO_2 samples, respectively, consistent with the XRD results (Fig. 1) that the sample with higher crystallinity has better defined long-range ordering. The cut-off distance indicates the average crystallite size of PC-TiO_2 and FC-TiO_2 sample, which is also consistent with the XRD results calculated by the Scherrer equation.[45] The crystal structure of anatase TiO_2 is shown in Fig. 10b, where the O atoms, Ti atoms and TiO_6 octahedra are represented by red balls, black balls and blue planes. It has been reported that the Li ion diffusion pathway in anatase is along the empty zigzag TiO_6 channel (marked by purple arrow).[66,67] Note that the distance of the second-neighbor Ti–Ti shell (~3.8 Å, dashed black arrow) defines the size of the percolation pathway, which plays a significant role on Li^+ diffusion as well as the electrochemical performance.[59] The PDF profiles of laminated TiO_2 nanoparticle samples at the pristine state and charged state (delithiated) of the first cycle with the r range of 1–7 Å are shown in Fig. 10c. The first peak at ~2 Å corresponds to the first-neighbor Ti–O shell.[59] The peak at ~2.5 and ~3.0 Å corresponds to the first-neighbor O–O and Ti–Ti shell, respectively.[59] The peak at ~3.8 Å of the pristine samples is highlighted by dashed lines that represents the second-neighbor Ti–Ti shell across the Li^+ diffusion pathway. The peak positions of A-TiO_2, PC-TiO_2 and FC-TiO_2 samples are 3.75 Å, 3.83 Å and 3.85 Å, which increase with the increase of crystallinity. The shortened distance of Ti–Ti shell can possibly limit the available active sites and migration paths for Li^+ intercalation. Therefore, the A-TiO_2 sample shows the lowest specific capacity at low current rate (Fig. 5a). At the fully charged state where the Li ions are extracted from the structure, the peak position of the A-TiO_2, PC-TiO_2 and FC-TiO_2 samples shifted to 3.65 Å, 3.71 Å and 3.77 Å where the smallest shift is observed in FC-TiO_2 sample, indicating reversibility of the host structure. Moreover, the peaks of the A-TiO_2 at 3.65 Å and the PC-TiO_2 at 3.71 Å at the charged state changed significantly compared with the pristine state. Firstly, the peak became broad, indicating larger variance of Ti–Ti distance, which might be a result of disorders and defects induced by lithium insertion and extraction. Secondly, the integrated intensity became smaller, suggesting a decrease in Ti(IV) coordination number, which can be associated with the introduction of vacancies.[68] Moreover, the absence of the peak at ~2.5 Å for all TiO_2 samples at charged state suggests the ordering of O–O shell is interrupted. The PDF patterns at charged state should be identical to that at pristine state if the electrode is fully reversible. However, the significant change in peak shapes of the A-TiO_2 and PC-TiO_2 samples suggests a larger irreversibility, which possibly is due to Li ions becoming irreversibly trapped in the zigzag pathway after the 1st discharge process. The irreversible Li ion storage in A-TiO_2 and PC-TiO_2 samples is also consistent with their 1st cycle coulombic efficiency where the values of the A-TiO_2 (45%) and PC-TiO_2 (49%) samples are significantly smaller than that of the FC-TiO_2 sample (64%) (Fig. 4). In summary, Li insertion and extraction introduce disorder, defects and distortion to the original diffusion pathway after 1st charge.

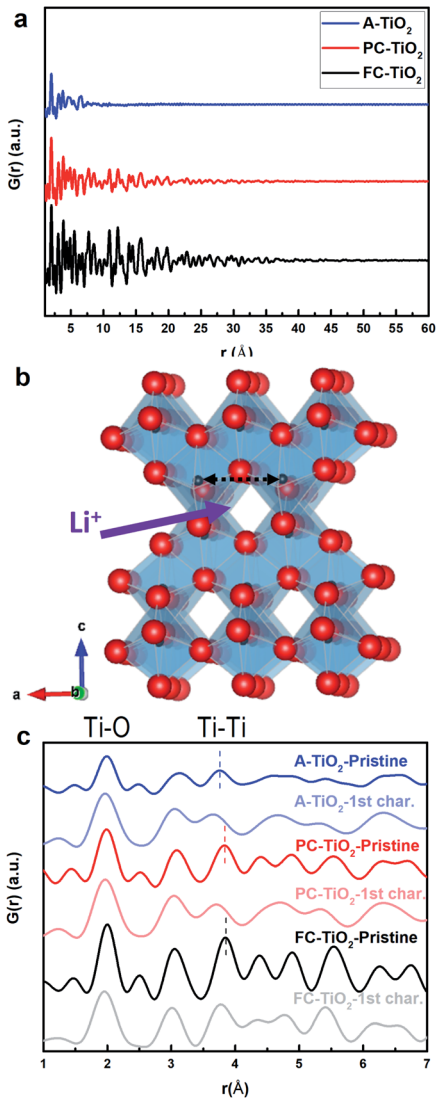

Fig. 10 PDF profiles of TiO_2 powder samples with the atomic distance ranged from 0 to 60 Å (a), the crystal structure of anatase TiO_2 (purple arrow: Li^+ diffusion pathway; black dashed line: the second-neighbour Ti–Ti shell) (b), and PDF profiles of laminated pristine and *ex situ* TiO_2 samples (c).

Conclusions

We successfully prepared amorphous, partially-crystalline and fully crystalline mesoporous TiO_2 spherical nanoparticles with a uniform size of 200 nm. The morphology and structure were confirmed by XRD and TEM. We evaluated the electrochemical performance of TiO_2 nanoparticle samples with varying crystallinity at both high and low current rates. At low current rate (quasi

steady-state), the specific capacity drops with the decrease of crystallinity where FC-TiO_2 and A-TiO_2 sample shows the highest and lowest capacity, respectively. The trend can be attributed to more available intercalation sites for TiO_2 nanoparticles with higher crystallinity. Moreover, it is possibly related to the lack of migration paths in disordered sample.[42] In addition, *ex situ* PDF analysis suggested that the 1D zigzag Li ion diffusion pathway becomes expanded with the increase of crystallinity. Compared to the A-TiO_2 and PC-TiO_2 samples, FC-TiO_2 has less trapped Li ions and more structural reversibility after the first cycle, leading to its high capacity at low current rate and better coulombic efficiency. In contrast, at high current rate, the A-TiO_2 sample shows slightly greater capacity than FC-TiO_2, both of which are much larger than the PC-TiO_2 sample. The charge storage and transport kinetics of TiO_2 nanoparticle electrodes were evaluated by CV, GITT and EIS. It was found that PC-TiO_2 had the lowest pseudocapacitive contribution and the lowest Li^+ diffusivity among all three samples, which explains its inferior rate capability compared to A-TiO_2 and FC-TiO_2 sample. A-TiO_2 shows the highest capacity at high current rate, which is associated with its high Li^+ diffusivity. The overall good rate capability of FC-TiO_2 can be ascribed to its high pseudocapacitive contribution as well as decent Li^+ diffusivity. Our study systematically unveiled how crystallinity impacts the electrochemical properties of mesoporous TiO_2 nanoparticle negative electrode materials for lithium ion batteries. Our results suggest that the phenomena observed in mesoporous solid TiO_2 nanoparticles might shed some lights on the crystallinity effect in intercalation-type metal oxide electrodes and support fundamental understanding of charge storage mechanisms in systems other than TiO_2 (*e.g.*, molybdenum oxide[35,36]). By carefully tuning the crystallinity in intercalation-type metal oxide electrode materials, it is possible to design electrode materials for different applications (*e.g.*, high energy *vs.* high power), which may provide a general strategy for the design of advanced oxide-based intercalation negative electrode materials.

Author contributions

HX and CD designed all experiments. YY designed the material synthesis. CD, DW, ML, CM, PS, JP, DJ, MD, BW and PB prepared the electrodes. YL and DH conducted TEM characterization. WX, HZ and YR conducted the synchrotron PDF experiments. XZ and DW designed and conducted the TGA/MS experiments. HX, CD, CM, WX, DW, DH, YY, and CZ analysed the data. All authors discussed the results and contributed to the manuscript preparation. HX, CD, DW, and WX wrote the manuscript.

Conflicts of interest

There are no conflicts to declare.

Acknowledgements

H. Xiong acknowledges support from the National Science Foundation under Grant No. DMR-1454984. C. Deng thanks the Hoffmann Institute of Advanced Materials (HIAM), Shenzhen Polytechnic for the postdoctoral fellowship. Yin was supported by UC Riverside and Korea Institute of Materials Science through the UC-KIMS Center for Innovation Materials for Energy and Environment and the Hydrogen Energy Innovation Technology Development Program of the National Research Foundation of Korea (NRF) funded by the Korean government (Ministry of Science and ICT (MSIT); Grant NRF-2019M3E6A1064020). The authors acknowledge TEM assistance by Xiaoju Li from State Key Laboratory of Microbial Technology at Shangdong University (China). The authors also thank Mr Eric Gabriel for reading the manuscript. Use of the Center for Nanoscale Materials, an Office of Science user facility, was supported by the U.S. Department of Energy, Office of Science, Office of Basic Energy Sciences, under Contract No. DE-AC02-06CH11357. This research used resources of the Advanced Photon Source, a U.S. Department of Energy (DOE) Office of Science User Facility operated for the DOE Office of Science by Argonne National Laboratory under Contract No. DE-AC02-06CH11357.

References

1 Y. Nishi, *J. Power Sources*, 2001, **100**, 101–106.
2 S. Goriparti, E. Miele, F. De Angelis, E. Di Fabrizio, R. P. Zaccaria and C. Capiglia, *J. Power Sources*, 2014, **257**, 421–443.
3 M. Broussely, P. Biensan and B. Simon, *Electrochim. Acta*, 1999, **45**, 3–22.
4 M. Aldissi, *J. Power Sources*, 2001, **94**, 219–224.
5 J. W. Wen, Y. Yu and C. H. Chen, *Mater. Express*, 2012, **2**, 197–212.
6 C. Uhlmann, J. Illig, M. Ender, R. Schuster and E. Ivers-Tiffee, *J. Power Sources*, 2015, **279**, 428–438.
7 D. Yaakov, Y. Gofer, D. Aurbach and I. C. Halalay, *J. Electrochem. Soc.*, 2010, **157**, A1383–A1391.
8 O. Yariv, D. Hirshberg, E. Zinigrad, A. Meitav, D. Aurbach, M. Jiang and B. R. Powell, *J. Electrochem. Soc.*, 2014, **161**, A1422–A1431.
9 Z. G. Yang, D. Choi, S. Kerisit, K. M. Rosso, D. H. Wang, J. Zhang, G. Graff and J. Liu, *J. Power Sources*, 2009, **192**, 588–598.
10 U. K. Sen, A. Shaligram and S. Mitra, *ACS Appl. Mater. Interfaces*, 2014, **6**, 14311–14319.
11 D. Deng, M. G. Kim, J. Y. Lee and J. Cho, *Energy Environ. Sci.*, 2009, **2**, 818–837.
12 C. P. Sandhya, B. John and C. Gouri, *Ionics*, 2014, **20**, 601–620.
13 K. J. Griffith, K. M. Wiaderek, G. Cibin, L. E. Marbella and C. P. Grey, *Nature*, 2018, **559**, 556–563.
14 V. Augustyn, P. Simon and B. Dunn, *Energy Environ. Sci.*, 2014, **7**, 1597–1614.
15 Y. Liu and Y. F. Yang, *J. Nanomater.*, 2016, 8123652.
16 H. Xiong, H. Yildirim, E. V. Shevchenko, V. B. Prakapenka, B. Koo, M. D. Slater, M. Balasubramanian, S. K. R. Sankaranarayanan, J. P. Greeley, S. Tepavcevic, N. M. Dimitrijevic, P. Podsiadlo, C. S. Johnson and T. Rajh, *J. Phys. Chem. C*, 2012, **116**, 3181–3187.

17 K. A. Smith, A. I. Savva, C. J. Deng, J. P. Wharry, S. Hwang, D. Su, Y. Q. Wang, J. Gong, T. Xu, D. P. Butt and H. Xiong, *J. Mater. Chem. A*, 2017, **5**, 11815–11824.
18 Z. Z. Yang, T. Xu, S. M. Gao, U. Welp and W. K. Kwok, *J. Phys. Chem. C*, 2010, **114**, 19151–19156.
19 B. Zachau-Christiansen, K. West, T. Jacobsen and S. Atlung, *Solid State Ionics*, 1988, **28**, 1176–1182.
20 L. Kavan, M. Gratzel, J. Rathousky and A. Zukal, *J. Electrochem. Soc.*, 1996, **143**, 394–400.
21 X. P. Gao, H. Y. Zhu, G. L. Pan, S. H. Ye, Y. Lan, F. Wu and D. Y. Song, *J. Phys. Chem. B*, 2004, **108**, 2868–2872.
22 M. A. Reddy, M. S. Kishore, V. Pralong, V. Caignaert, U. V. Varadaraju and B. Raveau, *Electrochem. Commun.*, 2006, **8**, 1299–1303.
23 L. Kavan, D. Fattakhova and P. Krtil, *J. Electrochem. Soc.*, 1999, **146**, 1375–1379.
24 A. R. Armstrong, G. Armstrong, J. Canales and P. G. Bruce, *J. Power Sources*, 2005, **146**, 501–506.
25 S. Brutti, V. Gentili, H. Menard, B. Scrosati and P. G. Bruce, *Adv. Energy Mater.*, 2012, **2**, 322–327.
26 M. A. Reddy, M. S. Kishore, V. Pralong, U. V. Varadaraju and B. Raveau, *Electrochem. Solid-State Lett.*, 2007, **10**, A29–A31.
27 R. K. B. Gover, J. R. Tolchard, H. Tukamoto, T. Murai and J. T. S. Irvine, *J. Electrochem. Soc.*, 1999, **146**, 4348–4353.
28 L. D. Noailles, C. S. Johnson, J. T. Vaughey and M. M. Thackeray, *J. Power Sources*, 1999, **81**, 259–263.
29 X. M. Yang, Y. C. Yang, H. S. Hou, Y. Zhang, L. B. Fang, J. Chen and X. B. Ji, *J. Phys. Chem. C*, 2015, **119**, 3923–3930.
30 A. Lamberti, N. Garino, A. Sacco, S. Bianco, A. Chiodoni and C. Gerbaldi, *Electrochim. Acta*, 2015, **151**, 222–229.
31 G. F. Ortiz, I. Hanzu, T. Djenizian, P. Lavela, J. L. Tirado and P. Knauth, *Chem. Mater.*, 2009, **21**, 63–67.
32 H. T. Fang, M. Liu, D. W. Wang, T. Sun, D. S. Guan, F. Li, J. G. Zhou, T. K. Sham and H. M. Cheng, *Nanotechnology*, 2009, **20**, 225701.
33 Y. Wang, Y. C. Zhu, Z. Xing and Y. T. Qian, *Int. J. Electrochem. Sci.*, 2013, **8**, 9851–9857.
34 J. Jang, S. M. Kim, Y. Kim, K. H. Park, J. H. Ku, J. H. Ryu and S. M. Oh, *Isr. J. Chem.*, 2015, **55**, 604–610.
35 B. K. Guo, X. P. Fang, B. Li, Y. F. Shi, C. Y. Ouyang, Y. S. Hu, Z. X. Wang, G. D. Stucky and L. Q. Chen, *Chem. Mater.*, 2012, **24**, 457–463.
36 Y. F. Shi, B. K. Guo, S. A. Corr, Q. H. Shi, Y. S. Hu, K. R. Heier, L. Q. Chen, R. Seshadri and G. D. Stucky, *Nano Lett.*, 2009, **9**, 4215–4220.
37 A. Kim, E. Park, H. Lee and H. Kim, *J. Alloys Compd.*, 2016, **681**, 301–306.
38 C. K. Christensen, A. Mamakhel, A. R. Balakrishna, B. B. Iversen, Y. M. Chiang and D. Ravnsbæk, *Nanoscale*, 2019, **11**, 12347.
39 H. Xiong, H. Yildirim, P. Podsiadlo, J. Zhang, V. B. Prakapenka, J. P. Greeley, E. V. Shevchenko, K. K. Zhuravlev, S. Tkachev, S. K. R. S. Sankaranarayanan and T. Rajh, *Phys. Rev. Lett.*, 2013, **110**, 078304.
40 H. Yildirim, J. P. Greeley and S. K. R. Sankaranarayanan, *ACS Appl. Mater. Interfaces*, 2014, **6**, 18962–18970.
41 N. Li, Q. Zhang, J. B. Joo, Z. D. Lu, M. Dahl, Y. Gan and Y. D. Yin, *Nanoscale*, 2016, **8**, 9113–9117.
42 F. Thoss, L. Giebeler, S. Oswald, H. Ehrenberg and J. Eckert, *Electrochim. Acta*, 2012, **60**, 85–94.
43 B. H. Toby and R. B. Von Dreele, *J. Appl. Crystallogr.*, 2013, **46**, 544–549.
44 P. Juhas, T. Davis, C. L. Farrow and S. J. L. Billinge, *J. Appl. Crystallogr.*, 2013, **46**, 560–566.
45 P. Scherrer, *Nachr. Ges. Wiss. Goettingen, Math.-Phys. Kl.*, 1918, **2**, 98–100.
46 R. A. Spurr and H. Myers, *Anal. Chem.*, 1957, **29**, 760–762.
47 S. T. Wang, W. Quan, Z. Zhu, Y. Yang, Q. Liu, Y. Ren, X. Y. Zhang, R. Xu, Y. Hong, Z. T. Zhang, K. Amine, Z. L. Tang, J. Lu and J. Li, *Nat. Commun.*, 2017, **8**, 1–8.
48 N. W. Liu, X. F. Guo, A. Navrotsky, L. Shi and D. Wu, *J. Catal.*, 2016, **342**, 158–163.
49 K. K. Ghuman, *Sci. Technol. Adv. Mater.*, 2018, **19**, 44–52.
50 F. X. Wu, Z. X. Wang, X. H. Li and H. J. Guo, *J. Mater. Chem.*, 2011, **21**, 12675–12681.
51 A. D. Roberts, X. Li and H. F. Zhang, *Chem. Soc. Rev.*, 2014, **43**, 4341–4356.
52 P. G. Bruce, B. Scrosati and J. M. Tarascon, *Angew. Chem., Int. Ed.*, 2008, **47**, 2930–2946.
53 Y. Ren, L. J. Hardwick and P. G. Bruce, *Angew. Chem., Int. Ed.*, 2010, **49**, 2570–2574.
54 J. W. Ma, W. Li, B. J. Morgan, J. Swiatowska, R. Baddour-Hadjean, M. Body, C. Legein, O. J. Borkiewicz, S. Leclerc, H. Groult, F. Lantelme, C. Laberty-Robert and D. Dambournet, *Chem. Mater.*, 2018, **30**, 3078–3089.
55 C. F. Liu, Z. G. Neale and G. Z. Cao, *Mater. Today*, 2016, **19**, 109–123.
56 V. Subramanian, A. Karki, K. I. Gnanasekar, F. P. Eddy and B. Rambabu, *J. Power Sources*, 2006, **159**, 186–192.
57 J. Wang, J. Polleux, J. Lim and B. Dunn, *J. Phys. Chem. C*, 2007, **111**, 14925–14931.
58 J. W. Kang, D. H. Kim, V. Mathew, J. S. Lim, J. H. Gim and J. Kimz, *J. Electrochem. Soc.*, 2011, **158**, A59–A62.
59 M. Fernandez-Garcia, C. Belver, J. C. Hanson, X. Wang and J. A. Rodriguez, *J. Am. Chem. Soc.*, 2007, **129**, 13604–13612.
60 H. Lindstrom, S. Sodergren, A. Solbrand, H. Rensmo, J. Hjelm, A. Hagfeldt and S. E. Lindquist, *J. Phys. Chem. B*, 1997, **101**, 7717–7722.
61 J. Wang, J. Polleux, J. Lim and B. Dunn, *J. Phys. Chem. C*, 2007, **111**, 14925–14931.
62 T. C. Liu, W. G. Pell, B. E. Conway and S. L. Roberson, *J. Electrochem. Soc.*, 1998, **145**, 1882–1888.
63 A. Van der Ven, J. Bhattacharya and A. A. Belak, *Acc. Chem. Res.*, 2013, **46**, 1216–1225.
64 L. Xin, Y. Liu, B. J. Li, X. Zhou, H. Shen, W. X. Zhao and C. L. Liang, *Sci. Rep.*, 2014, **4**, 4479.
65 V. Petkov, *Mater. Today*, 2008, **11**, 28–38.
66 M. Madian, A. Eychmuller and L. Giebeler, *Batteries*, 2018, **4**, 7.
67 J. A. Dawson and J. Robertson, *J. Phys. Chem. C*, 2016, **120**, 22910–22917.
68 V. Petkov, R. G. DiFrancesco, S. J. L. Billinge, M. Acharya and H. C. Foley, *Philos. Mag. B*, 1999, **79**, 1519–1530.